

Camera-Based Lane-Aided Multi-Information Integration for Land Vehicle Navigation

Xiaoji Niu , Yitang Peng, Yuhang Dai, Qijin Chen , Chi Guo , *Member, IEEE*,
and Quan Zhang , *Member, IEEE*

Abstract—Accurate positioning, especially lateral positioning, is an essential requirement of autonomous driving. Although high accuracy vehicle positioning can be conducted in open-sky environments by global navigation satellite system (GNSS), the positioning accuracy cannot be guaranteed in GNSS-denied environments such as urban canyons and tunnels. To solve this issue, inertial navigation systems, vehicle speed sensors, and vehicle motion constraints are often fused to mitigate positioning errors. However, this integration cannot meet the decimeter-level lateral positioning accuracy of autonomous vehicles' localization requirements. This article proposes a multi-information integration method aided by lane distance to further eliminate lateral error. In the proposed method, the lateral vehicle-to-lane distance measurements from camera-based systems, and the map-matching lane distance based on high-definition map were utilized to provide absolute lane distance measurement corrections in GNSS-denied environments. Field vehicular tests with low-cost integration systems were conducted to evaluate the navigation performance of the proposed multi-information integration method, and the results indicated that it is feasible for the proposed method to maintain continuous and reliable lateral positioning accuracy of better than 0.6 m under reliable lane line detection conditions in GNSS-denied environments.

Index Terms—Autonomous vehicles, lane distance, lateral positioning accuracy, low-cost integration systems, multi-information integration.

Manuscript received 10 March 2022; revised 7 June 2022; accepted 18 July 2022. Recommended by Technical Editor Y. Shtessel and Senior Editor K. J. Kyriakopoulos. This work was supported in part by the National Key Research and Development Program of China under Grant 2016YFB0502204, in part by the National Natural Science Foundation of China under Grant 42174024, and in part by the National Key Research and Development Program of China under Grant 2018YFC0809804. (Corresponding author: Quan Zhang.)

Xiaoji Niu, Qijin Chen, Chi Guo, and Quan Zhang are with the GNSS Research Center, Wuhan University, Wuhan 430079, China, and also with the Hubei Luoja Laboratory, Wuhan 430079, China (e-mail: xjniu@whu.edu.cn; chenqijin@whu.edu.cn; guochi@whu.edu.cn; zhangquan@whu.edu.cn).

Yitang Peng and Yuhang Dai are with the GNSS Research Center, Wuhan University, Wuhan 430079, China (e-mail: yitangp@whu.edu.cn; daiyuhang@whu.edu.cn).

Color versions of one or more figures in this article are available at <https://doi.org/10.1109/TMECH.2022.3192985>.

Digital Object Identifier 10.1109/TMECH.2022.3192985

I. INTRODUCTION

WITH the rapid development of autonomous driving technology, robust and accurate vehicle navigation and positioning technologies have attracted the significant attention in the last decade. For open-sky environments, the global navigation satellite system (GNSS) has proven to be a reliable and efficient positioning technology, which can even provide centimeter-level positioning based on the real-time kinematics (RTK) technology [1]. However, GNSS positioning solution cannot overcome signal blockages, multipath effects, and limited visible satellites in GNSS-denied environments, which cause poor positioning accuracy or the inability to position. To obtain stable and reliable positioning solutions, GNSS is often integrated with inertial navigation system (INS) because of its complementary characteristics. However, inertial navigation errors drift over time due to sensor errors; thus GNSS/INS integration cannot maintain continuous high-precision positioning capability for a long time in many GNSS-denied areas such as tunnels or overheads [2], [3]. In particular, the low-cost microelectromechanical-system (MEMS) inertial measurement unit (IMU) can experience large position and attitude errors over short time intervals, which are mainly from large uncertainties in the MEMS IMU sensor output. Therefore, the INS built on these sensors is vulnerable to nonlinear error behavior [4].

To overcome the drawbacks of the GNSS/INS integrated navigation system in land vehicle navigation applications, vehicle speed sensors and vehicle motion constraints are often fused to mitigate positioning errors [3], [4]. With the development of camera-based sensing techniques, the image information provided by computer vision algorithms have been used in multi-information integration. Such image cues can be fused for localization and navigation. For example, some studies have focused on GNSS/INS/camera fusion systems by integrating lane features through a particle filter [5]–[8]. However, the majority of these lane-feature-based integration schemes either lack reliable positioning accuracy in GNSS-denied environments or depend on many empirical parameters. However, lane markings can be used as topological and geometrical information in map-based localization methods, as described in previous literature [9]–[13], lateral vehicle-to-lane distance as can be used as the main measurement information in improving the positioning accuracy. Rose et al. [9] designed a navigation filter to integrate the lateral lane distance measurement based on a camera with a GNSS/INS system. Gruyer et al. [10] proposed

TABLE I
COMPARISON OF DIFFERENT METHODS

Integration Method	Coupled Mode	Algorithm Description	Characteristics
Features-based	Tightly	Particle filter with a high computational cost is utilized for pose estimation based on the lane line.	Sub-meter level , but much reliance on the empirical parameters.
Current lane marking-based	Loosely	Position information obtained by the matching processing between the lane line and the map is taken as the observation.	Decimeter level , and the map matching with the lane line.
Proposed lane marking-based	Tightly	Lane line distance identified by the camera is taken as the observation.	Sub-decimeter level , and the map matching without lane line.

a similar approach to improve GNSS/INS/odometer (ODO) positioning accuracy using lateral lane detection information. However, most of these map-based positioning methods did not fully consider the characteristics of the GNSS/INS system and only loosely regard lateral lane distance as a measurement for calculating lateral position drift. The GNSS/INS and the lane detection systems are usually considered as two independent modules. A comparison of the different methods is given in Table I.

Bing able to tightly append the lateral vehicle-to-lane distance measurements to the GNSS/INS system and to take full advantage of lane constraints is crucial. To achieve tightly coupled integration, this article directly regarded the lateral lane distance measurements detected by a camera and high-definition (HD) map as accurate measurements to construct a lane-aided positioning algorithm. In particular, when GNSS signals were interrupted or blocked, the lateral positioning accuracy of the multi-information system aided by lane distance was successfully stabilized at the decimeter level instead of deteriorating with the growing error drift of the INS. Simultaneously, the vehicle velocities from the ODO and motion constraints were utilized to suppress the divergence of INS navigation, which provided more accurate navigation results for map matching (MM) in GNSS-denied environments. Compared to the current methods, the main contributions of this article can be summarized as follows: first, the raw lane line distance detected by the camera rather than the position was directly selected as the observation for precise pose estimation, and the camera information should not be applied for the MM to reduce the influence of the camera observation error; and second, the multisensor fusion aided by the ODO and motion constraints, which replaced the GNSS-only mode, was utilized to guarantee the accuracy of the MM in GNSS-denied environments.

The rest of the article is organized as follows: Section II introduces the basic principles of the GNSS/INS/ODO integration system, and Section III expounds the tightly-coupled lane-aided integration algorithm where the mathematical formula of the lane-aided positioning algorithm and the physical model are presented. In Section IV, the field vehicular tests and data processing strategies are described, and the experimental results

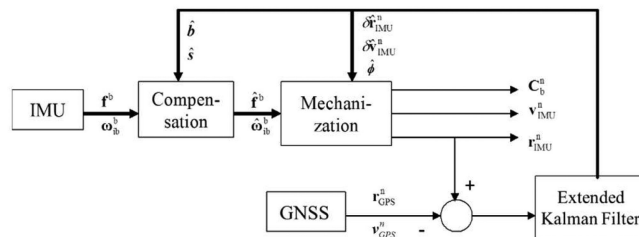


Fig. 1. Algorithm frame of loosely-coupled GNSS/INS integration.

are analyzed and discussed. The advantages of the proposed multi-information fusion positioning algorithm are summarized in Section V.

II. GNSS/INS/ODO INTEGRATION ALGORITHM

The lane-aided positioning algorithm was fused into the mature GNSS/INS/ODO navigation system, which made it necessary to introduce a basic integration algorithm that included basic GNSS/INS integration and a vehicle velocity-aiding algorithm.

A. Basic Frame of GNSS/INS Integration

The GNSS/INS integrated navigation algorithm comprised two parts: inertial mechanization and the extend Kalman filter (EKF). A detailed and comprehensive theoretical deduction of the inertial navigation algorithm was performed that has a basic technology widely utilized in aircraft, vehicles, ships, guided missiles, and other fields [14], [15]. The error analysis of the INS was established in the computer frame (c-frame, locally level at the computed position) or navigation frame (n-frame, local level frame), and the corresponding error analysis model was called the ψ angle error model or the ϕ angle error model. The relationship between the ϕ angle error formula and ψ angle error formula was fully compared and discussed [16].

The structure of the loosely-coupled GNSS/INS integration algorithm is shown in Fig. 1, where the position or velocity obtained by the GNSS system and estimated position or velocity of the inertial navigation algorithm were used as the input of the EKF. The measurement equation is designed with a loosely coupled closed-loop feedback mode, which enables estimation of the position, velocity, and attitude information of the vehicle as well as the state and IMU errors which can be fed back to the INS.

B. INS Mechanization and IMU Error Model

In a strapdown INS, an accelerometer is used to measure the specific force of the carrier relative to the inertial space and a gyroscope is used to measure the rotational angular velocity of the carrier relative to the inertial space.

Herein, the latitude and longitude were analyzed in angular form, and the altitude was differentiated separately. Savage and Shin comprehensively explained the standard inertial navigation algorithm. The INS mechanization equations can be summarized

as follows [14], [16]:

$$\begin{bmatrix} \dot{C}_n^e \\ \dot{h} \\ \dot{\mathbf{v}}^n \\ \dot{C}_b^n \end{bmatrix} = \begin{bmatrix} C_n^e (\boldsymbol{\omega}_{en}^n \times) \\ -v_D \\ C_b^n \mathbf{f}^b - (2\boldsymbol{\omega}_{ie}^n + \boldsymbol{\omega}_{en}^n) \times \mathbf{v}^n + \mathbf{g}_l^n \\ C_b^n (\boldsymbol{\omega}_{ib}^b \times) - (\boldsymbol{\omega}_{in}^n \times) C_b^n \end{bmatrix} \quad (1)$$

where \mathbf{f}^b represent the specific force in the body frame (b-frame, forward-right-down, abbreviated as FRD), \mathbf{v}^n represent velocity in the navigation frame [n-frame, North-East-Down, (NED)], C_n^e is the rotation matrix from navigation frame to earth frame (e-frame, fixed with respect to the Earth), C_b^n is the rotation matrix from body frame to navigation frame, \mathbf{g}_l^n is the normal gravity in the local position in the n -frame, $\boldsymbol{\omega}_{ib}^b$ is the angular rate of b -frame relative to inertial frame (i-frame, nonrotating with respect to the Earth) in the b -frame, $\boldsymbol{\omega}_{nb}^b$ is the angular rate of b -frame relative to n -frame in the b -frame, $\boldsymbol{\omega}_{in}^n$ is the angular rate of n -frame relative to i -frame in the n -frame, $\boldsymbol{\omega}_{en}^n$ is the angular rate of n -frame relative to e -frame in the n -frame, $\boldsymbol{\omega}_{ie}^n$ is the angular rate of e -frame relative to i -frame in the n -frame, and $\boldsymbol{\omega}_{ie}^e$ is the angular rate of e -frame relative to i -frame in the e -frame and h is the ellipsoid height.

As shown in Fig. 1, the angular rates output by the gyroscope were integrated into the attitude, and then the specific force output by the accelerometer was transformed into an n -frame with attitude information. In addition, the specific force needed to be transformed to real acceleration using the earth gravity compensation model. Subsequently, the acceleration could be integrated into the velocity, and further integrated into the position.

After estimating the state information, such as position, velocity, and attitude, it is necessary to conduct a model analysis of the estimated navigation error. In this article, the error perturbation analysis method is used to analyze the INS ψ angle error model. This method performed Taylor expansion around the true value of the navigation parameters, removed the high-order term error, and obtained the error differential equation as follows:

$$\begin{cases} \delta \dot{\mathbf{r}}^c = -\boldsymbol{\omega}_{ec}^c \times \delta \mathbf{r}^c + \delta \mathbf{v}^c \\ \delta \dot{\mathbf{v}}^c = \mathbf{f}^c \times \psi_{cp} + C_b^n \delta \mathbf{f}^b - (2\boldsymbol{\omega}_{ie}^c + \boldsymbol{\omega}_{ec}^c) \times \delta \mathbf{v}^c + \delta \mathbf{g}_l^c \\ \dot{\psi}_{cp} = -\boldsymbol{\omega}_{ic}^c \times \psi_{cp} - C_b^n \delta \boldsymbol{\omega}_{ib}^b \end{cases} \quad (2)$$

where δ represents variable error, $\delta \mathbf{r}^c$ is position errors in c -frame, and $\delta \mathbf{v}^c$ represents velocity errors in c -frame. Finally, the velocity error $\delta \mathbf{v}^c$ can be transformed to $\delta \mathbf{v}^n$ with following equation:

$$\delta \mathbf{v}^n = \delta \mathbf{v}^c - \delta \boldsymbol{\theta} \times \mathbf{v}^n. \quad (3)$$

The measurement data of inertial sensors contain many errors, such as bias, scale factor, and nonorthogonality errors. Calibration usually eliminates constant error, although the residual random errors of the inertial sensors must be estimated and compensated in the EKF. The main residual errors include gyro bias \mathbf{b}_g , accelerometer bias \mathbf{b}_a , gyro scale factor s_g , and accelerometer scale factor s_a . A continuous first-order Gaussian Markov process is suitable for the residual inertial sensor error,

as follows:

$$\dot{\mathbf{x}}(t) = -\frac{1}{T} \mathbf{x}(t) + \mathbf{w}(t) \quad (4)$$

where $\mathbf{x}(t)$ represents the residual error of the inertial sensors, and $\mathbf{w}(t)$ is the driving white noise. Combining the simplified IMU error model based on the ψ angle model and (4) yields the 21-dimensional (21-D) error states equation as follows:

$$\mathbf{x}_k = \Phi_{k,k-1} \mathbf{x}_{k-1} + \mathbf{G}_{k-1} \mathbf{w}_{k-1} \quad (5)$$

$$\mathbf{x} = [\delta \mathbf{r}_{INS}^c \quad \delta \mathbf{v}_{INS}^c \quad \psi \quad \mathbf{b}_g \quad \mathbf{b}_a \quad s_g \quad s_a]^T \quad (6)$$

where $\Phi_{k,k-1}$ is the state transformation matrix, \mathbf{G}_{k-1} is the noise matrix, \mathbf{w}_{k-1} is the driving white noise, and \mathbf{x} is the 21-D error state vector.

Moreover, the measurement equation can be described as

$$\mathbf{z}_k = \mathbf{H}_k \mathbf{x}_k + \delta \mathbf{n}_k \quad (7)$$

where \mathbf{z}_k is the measurement vector, \mathbf{H}_k is the measurement matrix, and $\delta \mathbf{n}_k$ is the measurement noise.

C. GNSS Measurement Equation

The relative position equation between the antenna phase center of the GNSS receiver and the IMU measurement center can be written as

$$\mathbf{r}_{GNSS}^n = \mathbf{r}_{IMU}^n + \mathbf{D}_R^{-1} C_b^n \mathbf{l}_{GNSS}^b \quad (8)$$

where \mathbf{l}_{GNSS}^b is the lever arm offset vector of the GPS antenna from the center of the IMU in the body frame, \mathbf{D}_R^{-1} is used to transform the north-east-down meters in the navigation frame into latitude, longitude, and height, and \mathbf{r}_{GNSS}^n denotes the true position of the GNSS antenna phase center.

The estimated position of the phase center of the GNSS antenna was derived from the estimated IMU position and lever arm offset vector using error perturbation analysis method

$$\hat{\mathbf{r}}_{GNSS}^n = \mathbf{r}_{GNSS}^n + \mathbf{D}_R^{-1} \delta \mathbf{r}_{IMU}^n + \mathbf{D}_R^{-1} (C_b^n \mathbf{l}_{GNSS}^b \times) \boldsymbol{\phi} \quad (9)$$

where $\boldsymbol{\phi}$ can be written as

$$\boldsymbol{\phi} = \psi + \delta \boldsymbol{\theta} \quad (10)$$

where $\delta \boldsymbol{\theta}$ is a small angle difference.

The position measurement of the phase center of the GNSS antenna is

$$\tilde{\mathbf{r}}_{GNSS}^n = \mathbf{r}_{GNSS}^n - \mathbf{D}_R^{-1} \mathbf{n}_{rG} \quad (11)$$

where \mathbf{n}_{rG} represent measurement position noise.

The measurement vector can be written as the difference between the estimated position and the measurement position of the phase center of the GNSS antenna

$$\mathbf{z}_{rGNSS} = \mathbf{D}_R (\hat{\mathbf{r}}_{GNSS}^n - \tilde{\mathbf{r}}_{GNSS}^n) = \delta \mathbf{r}_{IMU}^n + (C_b^n \mathbf{l}_{GNSS}^b \times) \boldsymbol{\phi} + \mathbf{n}_{rG} \quad (12)$$

$$\mathbf{H}_{rGNSS} = [\mathbf{I}_3 \quad \mathbf{0}_3 \quad (C_b^n \mathbf{l}_{GNSS}^b \times) \quad \mathbf{0}_3 \quad \mathbf{0}_3 \quad \mathbf{0}_3 \quad \mathbf{0}_3] \quad (13)$$

where \mathbf{z}_{rGNSS} is GNSS measurement vector and \mathbf{H}_{rGNSS} is the measurement matrix.

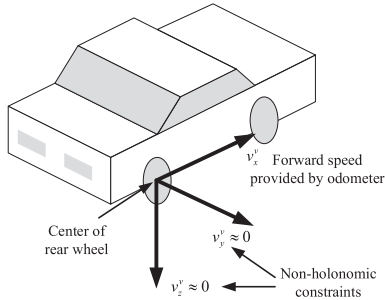


Fig. 2. Vehicle velocity-aided model based on ODO and NHCs.

D. Vehicle Velocity-Aiding Algorithm

In the vehicle motion model, the ODO and nonholonomic constraint (NHC) can be combined to construct a 3-D velocity-aiding algorithm, although the NHC only works on a land vehicle platform, and assumes that if the vehicle does not jump off the ground or slide sideways under normal conditions, the velocities of the vehicle in the plane perpendicular to the forward direction are approximately zero [17]. The ODO measures the forward speed of the vehicle in the vehicle frame (v -frame).

The vehicle velocity-aiding model is shown in Fig. 2, where the vehicle measurement velocity can be set at the ODO point, and the 3-D velocity vector can be written as

$$\mathbf{v}^v = [v_x^v \quad v_y^v \quad v_z^v]^T \approx [\tilde{v}_x^v \quad 0 \quad 0]^T. \quad (14)$$

Subsequently, the vehicle velocity in the vehicle frame (v -frame, forward-right-down, FRD) \mathbf{v}^v can be deduced from the INS navigation information as follows:

$$\mathbf{v}^v = \mathbf{C}_b^v \mathbf{C}_n^b \mathbf{v}_{\text{IMU}}^n + \mathbf{C}_b^v (\boldsymbol{\omega}_{nb}^b \times) \mathbf{l}_{odo}^b \quad (15)$$

where \mathbf{l}_{odo}^b is the lever arm offset vector from the ODO to the center of the IMU in the body frame and \mathbf{C}_b^v is the rotation matrix from the body frame to the vehicle frame.

The estimated vehicle velocity $\hat{\mathbf{v}}^v$ at the ODO point can be derived from the center of the IMU using the error perturbation analysis method as follows:

$$\hat{\mathbf{v}}^v = \mathbf{v}^v + \mathbf{C}_b^v \mathbf{C}_n^b \delta \mathbf{v}^n - \mathbf{C}_b^v \mathbf{C}_n^b (\mathbf{v}_{\text{IMU}}^n \times) \boldsymbol{\phi} - \mathbf{C}_b^v (\mathbf{l}_{odo}^b \times) \delta \boldsymbol{\omega}_{ib}^b. \quad (16)$$

The velocity measurement $\tilde{\mathbf{v}}^v$ can be written as

$$\tilde{\mathbf{v}}^v = \mathbf{v}^v + \mathbf{e}_v \quad (17)$$

where \mathbf{v}^v means the true vehicle velocity and \mathbf{e}_v is measurement error.

Considering (16) and (17), the velocity measurement equation can be constructed as follows:

$$\begin{aligned} \mathbf{z}_{odo} &= \hat{\mathbf{v}}_{odo}^v - \tilde{\mathbf{v}}_{odo}^v \\ &= \mathbf{C}_b^v \mathbf{C}_n^b \delta \mathbf{v}^n - \mathbf{C}_b^v \mathbf{C}_n^b (\mathbf{v}_{\text{IMU}}^n \times) \boldsymbol{\phi} - \mathbf{C}_b^v (\mathbf{l}_{odo}^b \times) \delta \boldsymbol{\omega}_{ib}^b - \mathbf{e}_v \end{aligned} \quad (18)$$

where \mathbf{z}_{odo} represents the velocity measurement, which is the difference between the estimated and measured velocities. Therefore, the corresponding measurement matrix \mathbf{H}_{vel} can be

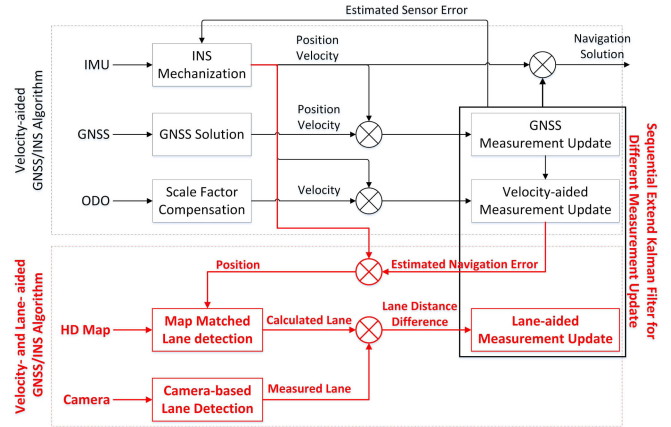


Fig. 3. Multi-information fusion frame aided by the lane distance from camera and HD map.

written as

$$\mathbf{H}_{vel} = \begin{bmatrix} \mathbf{0}_3 & \mathbf{C}_b^v \mathbf{C}_n^b & -\mathbf{C}_b^v \mathbf{C}_n^b (\mathbf{v}_{\text{IMU}}^v \times) & -\mathbf{C}_b^v (\mathbf{l}_{wheel}^b \times) \\ \mathbf{0}_3 & -\mathbf{C}_b^v (\mathbf{l}_{wheel}^b \times) \cdot \text{diag}(\boldsymbol{\omega}_{ib}^b) & \mathbf{0}_3 \end{bmatrix}. \quad (19)$$

The velocity-aided algorithm was constructed using the speed provided by the ODO and motion constraints (e.g., NHC). When the velocity-aided positioning algorithm worked together with the INS algorithm, the algorithm was referred as the velocity-aided INS algorithm. It should be noted that the sequential EKF for different measurement updates was applied later because the different data rates of multisource information, and this frame design can guarantee the plug-and-play of multiple observation information.

III. LANE-AIDED POSITIONING TECHNOLOGY

To further solve the positioning errors drift in long-term GNSS-blocked environments, the vehicle-to-lane distance needed to be integrated with the GNSS/INS/ODO navigation system to construct a comprehensive multi-information fusion system. Fig. 3 shows the proposed multi-information fusion frame aided by the lane distance from the camera and HD map, which is divided into four parts. First, the navigation information provided by the GNSS/INS/ODO integration module was combined with the pre-built HD map to obtain the map-matched lateral lane distance. Second, the monocular camera module was activated to provide the recognized lateral lane distance. Third, the difference between the map-matched lane distance and the recognized lane distance was obtained to construct the measurement and observation equations. Finally, the sequential EKF was replenished with the lane-aided positioning algorithm, which can effectively suppress the lateral position error divergence.

This article mainly used lateral distance information from the vehicle to the lateral lane, which is referred to herein as the lateral lane distance. The lateral lane distance was obtained in two ways: The first method utilized a monocular camera to identify the lane and calculate the lateral lane distance using computer vision technology [18]–[21]. This method is characterized by high precision and no dependence on other sensors or data sources;

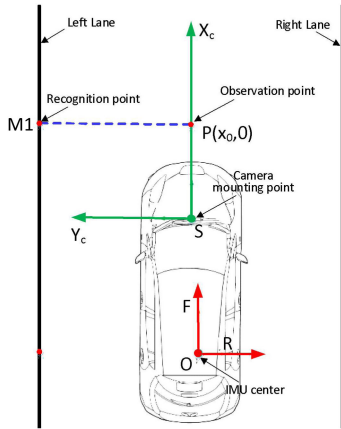


Fig. 4. Camera-based lateral lane recognition model.

the second method was to calculate the lateral lane distance by means of MM and the projection method based on an HD map and estimated vehicle position. The accuracy of the lateral lane distance obtained using the second method mainly depended on the accuracy of the estimated vehicle position.

A. Camera-Based Lateral Lane Distance

Considering that lane detection is a mature technology in computer vision, we did not study lane detection technology in depth, but utilized the commercial lane detection system to obtain lane distance. Lane detection usually requires placing a monocular camera behind the windshield of the vehicle and transmitting the image information captured by the camera to the embedded processor on the vehicle. The system can then output the lane information recognized by the camera with the built-in lane recognition algorithm.

The great advances in lane detection technology have mainly been attributed to lane departure warning systems (LDWS) [22]. To describe the lane mathematically, Kluge proposed a camera system that can provide the lane marking parameters of the Taylor expansion of a clothoid in the camera coordinate system [23]

$$f(x) = c_0 + c_1x + c_2x^2 + c_3x^3 \quad (20)$$

where the coefficients c_0 , c_1 , c_2 , and c_3 are the lateral distance, slope, curvature, and curvature derivative of the detected lane markings, respectively.

In this section, we simplify the lane detection model and adjust the camera system to that of an actual vehicular platform. Theoretically, the lateral lane includes the left and right lane, and a lane-aided algorithm can be constructed with either one. In this article, however, we adopt the left lane as the lateral lane.

The mathematical model of the lane detection module is shown in Fig. 4, where point O is the center of the IMU, and point S represents the position of the installed monocular camera. The monocular camera uses point S as the origin of the camera coordinate system; the forward direction of the vehicle is the X-axis, and the lateral direction is the Y-axis in the camera coordinate system.

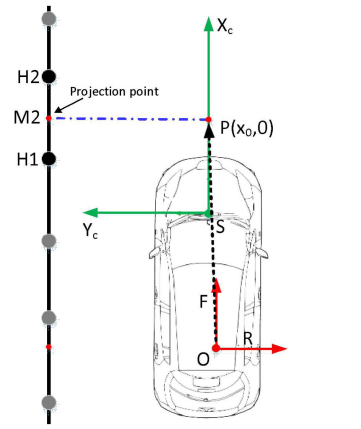


Fig. 5. Map-matched lateral lane prediction model.

Point P is the measurement point in front of the camera and changes with the movement of the vehicle. Point M is the projection point of point P on the left-hand lane. During the lane recognition process, the lateral lane distance output by the monocular camera system was PM_1 . The coordinates of point P in the camera frame (x_0) could also be output by a monocular camera system.

B. Map Matched Lateral Lane Distance

The purpose of the MM algorithm was to match the vehicle position and trajectory estimated by the positioning system with the road line in the HD map (the range error allowed for the HD digital map is ± 0.15 m). The vehicle position was then projected onto the road segment in the HD map [24]–[26]. The map-matching method used in this article was a relatively simple, essential, and robust projection and matching scheme, as shown in Fig. 5. First, the GNSS/INS/ODO integration system was used to estimate the vehicle position. Second, combined with the HD map, MM technology was used to find the lateral lane matching the current estimated vehicle position. Finally, the vehicle position was projected onto the lane to obtain the coordinate of the projection point, which allowed the lateral lane distance to be calculated.

As shown in Fig. 5, l_{OP} is the lever arm offset vector from the IMU to the camera detection point P projected in the b-frame (we assume that the camera coordinate frame is strictly aligned with the vehicle frame in this article).

The MM model for calculating lateral lane distance are summarized as follows.

- 1) The position of the IMU can be easily estimated using the GNSS/INS integrated navigation algorithm, and the position of point P was solved using the lever arm compensation method

$$r_P^n = r_{IMU}^n + D_R^{-1} C_b^n l_{OP}. \quad (21)$$

- 2) After estimating the position of point P, the current vehicle lane in the HD Map was determined using map-matching algorithm.
- 3) According to the coordinates of H1 and H2, which are the points to describe the matched lane extracted from

the HD map, and combined with point P , the coordinates of the projection point ($M2$) of point P could be calculated using the mathematical projection method.

- 4) Finally, the map-matched lateral lane distance could be calculated according to the coordinates of point P and projection point $M2$.

C. Lane-Aided Model

It is necessary to construct a linearized measurement model to apply Kalman filter to improve the positioning accuracy of GNSS/INS/ODO by using both the recognized lateral lane distance from a monocular camera and the map-matched lateral lane distance. Compared to the methods in previous studies that mainly focused on lane keeping, the proposed model in this article seeks to improve the absolute positioning accuracy of the entire navigation system by involving the road lane coordinate information from HD map.

To simplify our lane-aided model (LAM), we make and adhered to the following declarations to ensure that errors are correctly compensated.

- 1) Calibration and compensation of the sensor installation angle and lever arm must be performed to maintain a consistent coordinate system to reduce the effect of space asynchronism.
- 2) Time synchronization among GNSS RTK, MEMS IMU, ODO and monocular camera modules needs to be implemented to reduce the effect of time asynchronism.
- 3) LAM model is mainly based on an approximate straight line and does not fully function in a severely curved lane. This is because the recognized lateral lane distance at a severely curved corner is not easily consistent with map-matched lateral lane distances.

It should be noted that the simplified lane-aided mode is based on some limited conditions. It could be applied to normal vehicle driving conditions, but it may not perform well in the absence of declarative conditions. The weight adjustment and optimization of observation information should be considered when applying this mode to reduce the influence caused by model on the applicability for all scenarios.

The simplified LAM is shown in Fig. 6, where O indicates the installed IMU, S represents the installed camera, the X - and Y -axes indicate the directions of the camera coordinate system, P is the detection point of the monocular camera, PM_1 indicates the lateral lane distance detected by the monocular camera system, and PM_2 indicates the map-matched lateral lane distance.

We set the map-matched lateral lane distance vector L_{MM}^v (MM) as follows:

$$L_{MM}^v = [x \quad y \quad z]^T \quad (22)$$

where x , y , and z , respectively, present the distance vector in forward-right-down directions, and the lateral lane distance y is considered

$$y = PM_2 \quad (23)$$

where PM_2 is map-matched lane distance.

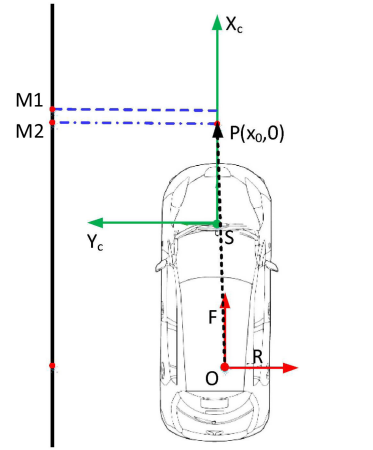


Fig. 6. LAM through camera and HD map.

The map-matched lane distance vector L_{MM}^v can be calculated using the known coordinates of points P and $M2$

$$L_{MM}^v = C_b^v C_n^b D_R (r_P^n - r_{M2}^n) \quad (24)$$

where r_P^n denotes the coordinates of point P in the latitude, longitude, and height frame; r_{M2}^n denotes the coordinates of point $M2$ in the navigation frame, and C_n^b is the rotation matrix from the navigation frame to the body frame.

Simultaneously, the camera-recognized lateral lane distance vector \tilde{L}_{camera}^v can be written as

$$\tilde{L}_{camera}^v = [x \quad PM_1 \quad z]^T \quad (25)$$

where PM_1 is the recognized lateral lane distance of the monocular camera. The recognized lateral lane distance can be written as

$$\tilde{L}_{camera}^v = L_{camera}^v - e_c \quad (26)$$

where L_{camera}^v represents the true lateral lane distance and e_c is camera measurement noise.

Finally, the lane-aided measurement vector can be written as

$$z_{LAM} = \hat{L}_{MM}^v - \tilde{L}_{camera}^v \quad (27)$$

where \hat{L}_{MM}^v represents the map-matched lane distance vector, and z_{LAM} is the distance difference vector between the map-matched lane distance vector and the camera-recognized lane distance vector.

Substituting (21), (24), and (26) into (27) and performing error perturbation analysis, the lateral lane distance measurement equation can be written as

$$z_{LAM} = C_b^v C_n^b \delta r_{IMU}^n - C_b^v C_n^b [(D_R r_{IMU}^n - D_R r_{M2}^n) \times] \phi + e_c. \quad (28)$$

Then, the corresponding measurement matrix H_{LAM} is

$$H_{LAM} = [C_b^v C_n^b \mathbf{0}_3 - C_b^v C_n^b [(D_R r_{IMU}^n - D_R r_{M2}^n) \times] \mathbf{0}_3 \mathbf{0}_3 \mathbf{0}_3 \mathbf{0}_3]. \quad (29)$$

The experimental tests demonstrated that the accuracy of the distance from the vehicle to the lane line recognized by

TABLE II
PERFORMANCE SPECIFICATION OF THE IMU SENSORS

IMU sensors	Parameters	Tested system	Reference system
		MEMS IMU	EG320N IMU
Gyro	Bias ($^{\circ}/h$)	10	3.5
	ARW ($^{\circ}/\sqrt{h}$)	0.3	0.1
Accel.	Bias (mGal)	100	100
	VRW (m/s/ \sqrt{h})	0.05	0.05

TABLE III
LANE PARAMETERS OUTPUT BY MONOCULAR CAMERA

Name	Datatype	Units	Describe
Polynomial of the Left Lane	Float	m	$f(x) = c_0 + c_1x + c_2x^2 + c_3x^3$
X-axis Value of Detection Point	Float	m	x_0
Lateral Lane Distance	Float	m	$f(x_0)$

the camera is approximately 0.1 m. Therefore, the standard deviation of the lateral vehicle-to-lane distance observation was set to 0.1 m.

IV. EXPERIMENTS AND ANALYSIS

A. Multi-Information Fusion Hardware Platform

In this article, the navigation results of three positioning algorithms (the standalone INS algorithm, velocity-aided INS integration algorithm and the proposed lane- and velocity-aided INS integration algorithm) are compared. The navigation drift error relative to the reference solution under GNSS outages was used as a criterion to evaluate the performance of the proposed algorithm. Four field vehicular tests were conducted in an open-sky environment in Wuhan, China, in April 2019.

Low-cost GNSS/INS integrated navigation hardware with a UB4B0 GNSS receiver board and MEMS IMU was used as the test system. A NovAtel EG320N IMU with SPAN land vehicle technology mounted on the same vehicle was used as the reference system to provide the reference navigation solution. The detailed parameters of both IMUs are given in Table II.

A low-cost monocular camera lane recognition system from horizon robotics was used to recognize the lateral lane information. All lane parameters provided by the monocular camera system are given in Table III, and the recognized lateral lane distance can be calculated using the coordinates of point $P(x_0, 0)$ and the lane polynomial.

The monocular camera system was installed in the rearview mirror, and the MEMS IMU and EG320N were installed in the vehicle trunk, as shown in Fig. 7. Both the MEMS IMU and reference IMU obtained the same GNSS signal via the same GNSS receiver through a power splitter.

B. Field Tests and Analysis

When the vehicle moved in one of the directions indicated by the arrows in the open environment in Fig. 8, the multi-information system was able to obtain continuous GNSS signals

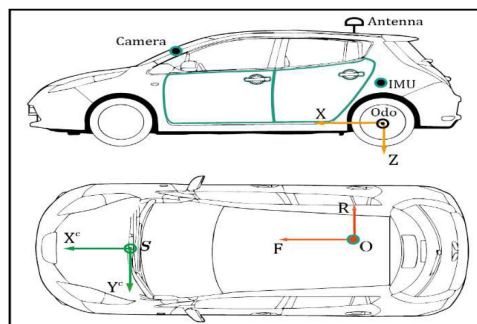


Fig. 7. Vehicular hardware test platform.



Fig. 8. Trajectory of field tests (here, numbers represent GNSS outages, and arrows indicate the direction of the vehicle).

with centimeter-level positioning accuracy (contributed by the RTK technology). Therefore, to evaluate the navigation performance improvement of the lane-aided positioning algorithm, the GNSS signals of the low-cost system were manually disconnected for 60 s numerous times during four field tests. Its maximum navigation errors (mainly including position and attitude errors) in comparison with those of the reference solutions during each GNSS outage were subsequently obtained. It should be emphasized that the backward-smoothed navigation solution of the reference system was used to ensure high navigation accuracy. Finally, we calculated the root-mean-square (RMS) values of the multiple maximum navigation errors in each field test. These values were used to evaluate the navigation accuracy of the multi-information fusion system.

Although there were 13 GNSS signals outages obtained in each field test all expressed numerically in Fig. 8, not all of them were used for performance analysis because some lane lines that were worn or obscured by objects could not be effectively detected. We utilized a total of 35 GNSS outages from the four field tests, covering approximately nine sections for each test, as shown in Fig. 9. The velocity and LAMs were both constructed in the vehicle frame, allowing for comparison of our LAM with the reference values, and for more rigorous verification of the proposed navigation algorithm's performance.

1) *One Field Vehicular Test*: Taking one field test as an example, we recorded the maximum position errors in multiple GNSS outages for the different algorithm modes, as shown in Fig. 9. There are three navigation algorithms from top to bottom to show the auxiliary effect of different external information: the

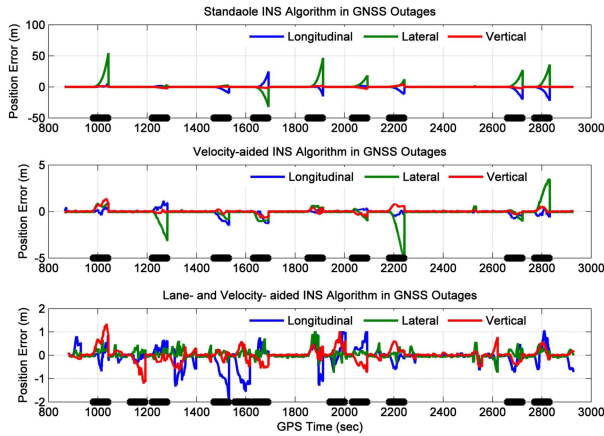


Fig. 9. Position drift error in 60 s GNSS outages for different integration modes.

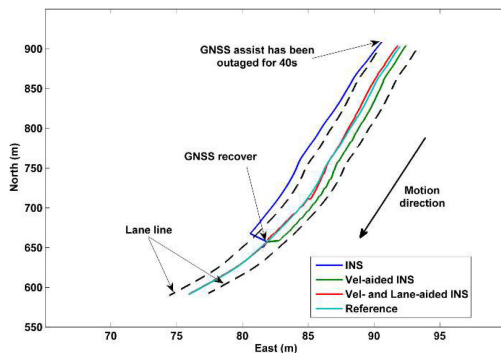


Fig. 10. Performance example of lane-level localization based on different integrated navigation modes during GNSS outages: slowly turning.

standalone INS algorithm; velocity-aided INS integration algorithm; and lane- and velocity- aided INS integration algorithm. The black sections in Fig. 9 represent the whole 60 s outages, and the remaining sections are GNSS available areas. As shown in Fig. 9, the maximum position errors of the standalone INS algorithm were controlled within 50 m, and was successfully reduced to within 5.0 m by adding the velocity-aided navigation mode. However, the lateral position errors of the velocity-aided INS algorithm for multiple GNSS outages could not reach the decimeter level of position accuracy. The lane- and velocity-aided INS algorithms shown in the third subgraph significantly reduce the lateral position errors within 1.0 m.

Figs. 10 and 11 show the horizontal positions of different positioning algorithms with two GNSS outages as an example to clearly demonstrate the lane-level localization capability of the proposed mode. Here, the lane lines were generated according to the road size, with the reference trajectory as the centerline. The INS mode alone could not remain within the lane lines when the GNSS assist was disable for 40 s. Although the velocity-aided INS mode resides within lane lines, the derived trajectory deviated significantly from the reference trajectory. The proposed lane- and velocity-aided INS mode not only resided within the lane lines, but also maintained the derived trajectory consistent with the reference trajectory.

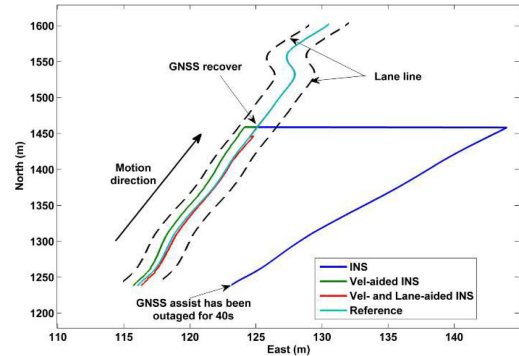


Fig. 11. Performance example of lane-level localization based on different integrated navigation modes during GNSS outages: going straight.

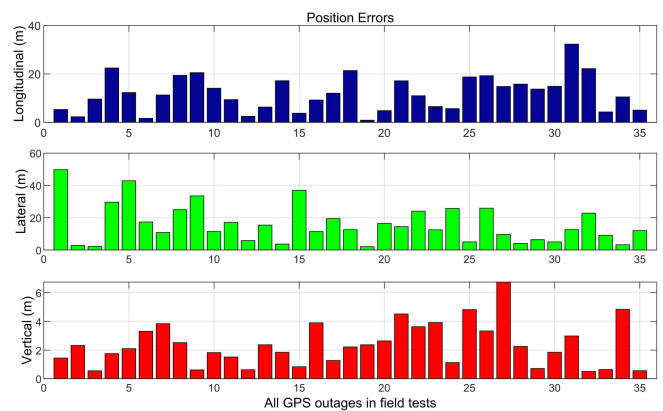


Fig. 12. Maximum position drift errors in 35 GNSS outages in the mode of standalone INS.

It can be drawn from the single filed test that the proposed multi-information fusion scheme in this article can achieve lateral positioning accuracy of better than 1.0 m in despite multiple GNSS outages, by integrating the velocity- and lane- aided positioning modules with a GNSS/INS algorithm. However, only one field test is insufficient for performance analysis, and statistical analysis based on many tests need to be performed to evaluate the positioning accuracy of the proposed algorithm. The following section presents the statistical analysis of the navigation performance in different modes through multiple field tests.

2) *Verification of Standalone-INS Algorithm Through Multiple Field Vehicular Tests:* Fig. 12 shows the maximum position drift errors of the INS mode alone during 35 GNSS outages including the longitudinal, lateral, and vertical errors in the vehicle frame. In this mode, the positioning accuracy was entirely determined by the IMU performance. The longitudinal and lateral errors were within approximately 50 m, and the height accuracy within 7.0 m.

Table IV gives the statistical maximum navigation drift error results of 35 GNSS outages in INS mode including position error and attitude error. The RMS values of the position errors in longitudinal, lateral, and vertical directions were about 13.71, 18.77, and 2.71 m respectively, and the attitude error RMS values

TABLE IV
STATISTICAL RESULTS OF MAXIMUM NAVIGATION DRIFT ERROR OF 35 GNSS OUTAGES IN THE MODE OF STANDALONE INS (RMS)

Test Number	Position Errors (m)			Attitude Errors (°)		
	Lon.	Lat.	Vert.	Roll	Pitch	Yaw
1	13.788	28.616	2.309	0.232	0.110	0.246
2	10.461	17.990	2.023	0.186	0.108	0.232
3	13.718	17.446	3.372	0.245	0.235	0.324
4	16.882	11.032	3.125	0.239	0.219	0.305
Average	13.712	18.771	2.707	0.226	0.168	0.277

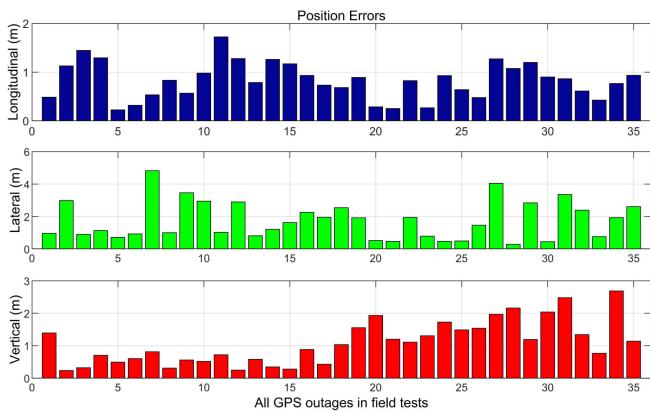


Fig. 13. Maximum position drift errors in 35 GNSS outages in the mode of velocity-aided INS.

in roll, pitch and yaw were about 0.226° , 0.168° , and 0.277° respectively.

3) Verification of Velocity-Aided Positioning Algorithm Through Multiple Field Vehicular Tests: As mentioned above, a vehicle velocity-aided positioning algorithm was designed to enhance the positioning performance of the integrated system. **Fig. 13** shows the maximum position drift errors in 35 GNSS outages in the velocity-aided INS algorithm, including the longitudinal, lateral, and vertical errors in the vehicle frame. It could be seen that the position errors in longitudinal, lateral and height are within approximately 2.0, 5.0, and 3.0 m respectively. Compared with **Fig. 12**, the position errors declined dramatically when the INS algorithm and the velocity-aided positioning algorithm worked together in GNSS-denied environments.

Table V gives the statistical results of the maximum navigation drift error of 35 GNSS outages in the velocity-aided INS algorithm. The RMS values of the position errors in longitudinal, lateral, and vertical directions are about 0.89, 2.04, and 1.14 m respectively, and the RMS values of the attitude errors in roll, pitch and yaw are about 0.141° , 0.123° , and 0.183° , respectively. Compared to those of the standalone INS algorithm (see **Table III**), the RMS values of the longitudinal position errors decreased from approximately 20 m to less than 1.0 m due to ODO measurements, while the reduction in lateral and vertical errors was attributed to NHC. The NHC also established the relationship between the velocity and attitude, which indicated that the attitude accuracy, particularly the yaw accuracy, could

TABLE V
STATISTICAL RESULTS OF MAXIMUM POSITION DRIFT ERROR OF 35 GNSS OUTAGES IN THE MODE OF VELOCITY-AIDED INS (RMS)

Test Number	Position Errors (m)			Attitude Errors (°)		
	Lon.	Lat.	Vert.	Roll	Pitch	Yaw
1	0.864	2.346	0.688	0.083	0.072	0.174
2	1.1484	1.993	0.542	0.085	0.060	0.116
3	0.637	1.402	1.459	0.197	0.202	0.205
4	0.930	2.422	1.860	0.198	0.174	0.237
Average	0.894	2.041	1.137	0.141	0.127	0.183

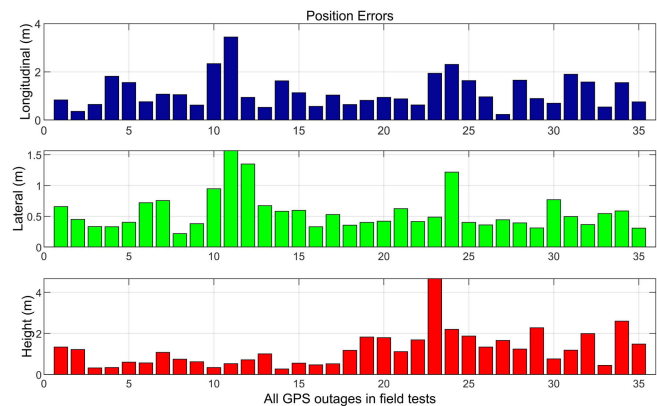


Fig. 14. Maximum position drift errors in 35 GNSS outages in the mode of lane-aided navigation integration.

be improved. However, decimeter-level lateral position accuracy was not achieved even when using the velocity-aided INS algorithm, and therefore needs to be further reduced in this algorithm.

4) Verification of Lane-Aided Positioning Algorithm Through Multiple Field Vehicular Tests: The detailed lane-aided positioning algorithm was described in the previous section. The lateral position error is a key parameter for evaluating the positioning performance of the lane-aided navigation algorithm in a multi-information fusion system.

Fig. 14 shows the maximum position drift errors in 35 GNSS outages in the lane-aided navigation integration mode, including the longitudinal, lateral, and vertical errors in the vehicle frame. The position errors in longitudinal, lateral, and height directions are within approximately 3.0, 1.5, and 4.0 m respectively. The lateral position error is obviously reduced from that presented in **Fig. 13**, and although the longitudinal position error and height error increased slightly, they remained relatively stable.

The statistics in terms of the navigation errors RMSs in the lane-aided navigation mode are given in **Table VI**. The average lateral position errors RMS value in 60 s GNSS outages was approximately 0.6 m, which was three times smaller than 2 m in the velocity-aided positioning system. It can be concluded that a significant improvement was achieved with the lane-aided positioning algorithm, and the best performance was obtained using a multi-information fusion scheme. The lane-aided navigation algorithm mainly provided absolute correction of the

TABLE VI

STATISTICAL RESULTS OF MAXIMUM POSITION DRIFT ERROR OF 35 GNSS OUTAGES IN THE MODE OF LANE-AIDED NAVIGATION INTEGRATION (RMS)

Test Number	Position Errors (m)			Attitude Errors (°)		
	Lon.	Lat.	Vert.	Roll	Pitch	Yaw
1	1.039	0.506	0.786	0.075	0.081	0.186
2	1.450	0.832	0.597	0.087	0.065	0.196
3	1.239	0.587	2.131	0.194	0.195	0.178
4	1.214	0.469	1.608	0.189	0.193	0.203
Average	1.236	0.599	1.281	0.136	0.134	0.191

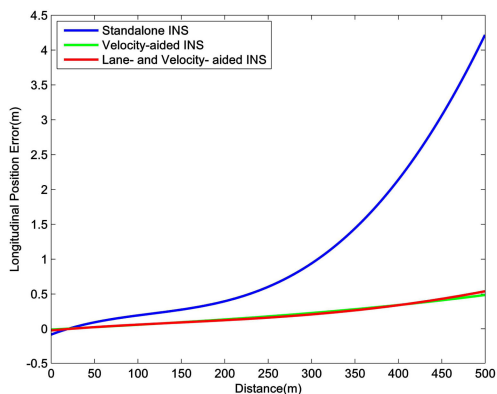


Fig. 15. Statistical results of longitudinal position error over distance travelled.

lateral position and had no strong relationship with the attitude. The attitude accuracy therefore remained basically unchanged.

The navigation errors in 60 s GNSS outages in different integration modes were analyzed through multiple field tests. The statistical results shows that the velocity information from the ODO and NHC were able to ensure the accuracy of the longitudinal position and attitude, and the lane information from the camera and HD map further improved the lateral position accuracy. The proposed multi-information fusion achieved lateral positioning accuracy of approximately 0.6 m.

5) *Summary of Position Errors Over Distance Travelled*: It is not intuitive to consider the relationship between the error drift of the three positioning algorithms with the GNSS outage time, therefore, analyzed the error characteristics of different positioning algorithms based on vehicle travelled distance instead of the GNSS outage time and showed the estimated error drift when no GNSS measurements were available.

Figs. 15–17 show the statistical longitudinal, lateral, and vertical position drift errors, respectively, over the travelled distance in the different integration modes. The blue line represents the error of the standalone INS algorithm in GNSS outages, which exhibited continual error growth in all axes owing to MEMS IMU sensor error. The green line represents the error of the velocity-aided INS algorithm during GNSS outages. Compared with the standalone INS algorithm, the velocity-aided positioning algorithm clearly improved the INS positioning accuracy, especially in the longitudinal and vertical directions. However, the lateral position error continued increase rapidly with

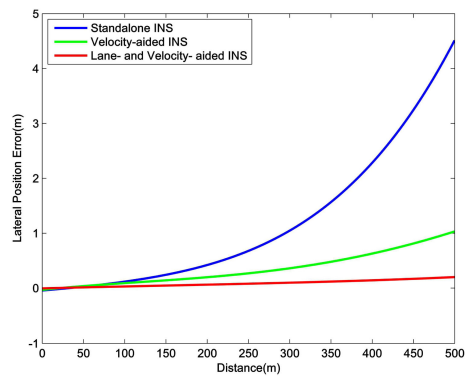


Fig. 16. Statistical results of lateral position error over distance travelled.

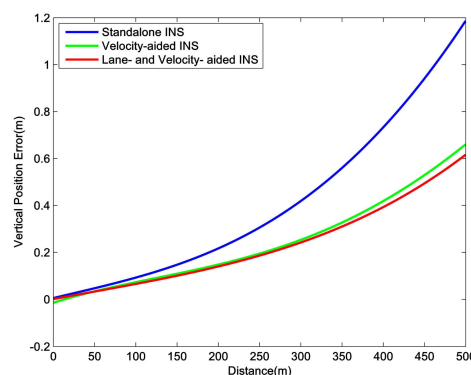


Fig. 17. Statistical results of vertical position error over distance travelled.

increasing distance. The red line represents the lane- and velocity-aided positioning algorithm, which significantly decreased the error drifts in GNSS outages in the three axes. From comparison to the velocity-aided INS algorithm, it can be concluded that the lane-aided mode limited the lateral error.

C. Comparative Statistics

Compared to the average RMS values of the position errors of the standalone INS algorithm in 60 s GNSS outages, the positioning accuracy of the proposed lane-aided INS algorithm was greatly improved.

To evaluate the positioning accuracy improvement ratio of the proposed lane-aided INS positioning algorithm, we defined the improvement ratio as

$$\text{Ratio} = \frac{\text{RMS}_{\text{INS}} - \text{RMS}_{\text{LAM}}}{\text{RMS}_{\text{INS}}} \times 100\% \quad (30)$$

where RMS_{INS} denotes the average RMS values of the maximum position errors in multiple GNSS outages for the standalone INS algorithm, and RMS_{LAM} represents the average RMS values of the maximum position errors in multiple GNSS outages for the proposed lane-aided INS positioning algorithm. The longitudinal, lateral, and vertical improvement ratios of positioning accuracy based on the proposed lane-aided INS positioning algorithm reached 91%, 96.8%, and 52.7%, respectively, as shown in Fig. 18.

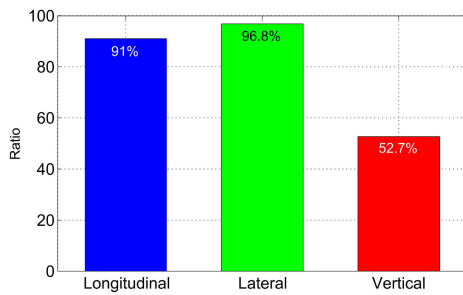


Fig. 18. Ratio of improved positioning accuracy by the proposed algorithm.

V. CONCLUSION

This article proposes a tightly coupled lane-aided GNSS/INS/ODO fusion algorithm that can obtain robust and precise positioning solution in long-term GNSS-denied environments. Considering that the velocity-aided positioning algorithm was mainly designed to restrain the longitudinal and vertical position errors and improve the attitude accuracy during GNSS outages. We propose the LAM to successfully increase the lateral position accuracy of better than 0.6 m during long-term GNSS outages.

To validate the proposed algorithm, four field vehicular tests were conducted and analyzed. Compared with the statistical values of the standalone INS positioning algorithm position errors during GNSS outages, those of the proposed lane-aided positioning algorithm indicate a positioning accuracy improvement of 91%, 96.8%, and 52.5% in the longitudinal, lateral, and vertical directions, respectively. When compared with the velocity-aided GNSS/INS positioning algorithm, the improvement ratio was still approximately 70% in the lateral positioning accuracy.

Moreover, some sensitivity analysis will be conducted to better optimize the proposed model, and more symbolic road marking should be utilized for better positioning accuracy despite long exposure to GNSS-denied environments. The robot datasets, including the corresponding processing results for public validation and analysis, and the download link, are available at: https://github.com/dyh996/Lane_Dataset.git.

REFERENCES

- [1] T. Li, H. Zhang, Z. Gao, X. Niu, and N. El-sheimy, "Tight fusion of a monocular camera, MEMS-IMU, and single-frequency multi-GNSS RTK for precise navigation in GNSS-Challenged environments," *Remote Sens.*, vol. 11, 2019, Art. no. 610.
- [2] Q. Zhang, X. Niu, H. Zhang, and C. Shi, "Algorithm improvement of the low-end GNSS/INS systems for land vehicles navigation," *Math. Probl. Eng.*, vol. 2013, pp. 1–12, 2013.
- [3] S. Godha and M. E. Cannon, "GPS/MEMS INS integrated system for navigation in urban areas," *GPS Solution*, vol. 11, pp. 193–203, 2007.
- [4] A. Noureldin, T. B. Karamat, M. D. Eberts, and A. El-Shafie, "Performance enhancement of MEMS-Based INS/GPS integration for low-cost navigation applications," *IEEE Trans. Veh. Technol.*, vol. 58, no. 3, pp. 1077–1096, Mar. 2009.
- [5] S. Kamijo, Y. Gu, and L. Hsu, "GNSS/INS/On-board camera integration for vehicle self-localization in urban canyon," in *Proc. IEEE 18th Int. Conf. Intell. Transp. Syst.*, 2015, pp. 2533–2538.
- [6] G. Panahandeh and M. Jansson, "Vision-Aided inertial navigation based on ground plane feature detection," *IEEE/ASME Trans. Mechatronics*, vol. 19, no. 4, pp. 1206–1215, Aug. 2014.
- [7] D. Kim, B. Kim, T. Chung, and K. Yi, "Lane-Level localization using an AVM camera for an automated driving vehicle in urban environments," *IEEE/ASME Trans. Mechatronics*, vol. 22, no. 1, pp. 280–290, Feb. 2017.
- [8] S. M. Zabihi, S. S. Beauchemin, E. A. M. de Medeiros, and M. A. Bauer, "Lane-Based vehicle localization in urban environments," in *Proc. IEEE Int. Conf. Veh. Electron. Saf.*, 2015, pp. 225–230.
- [9] C. Rose, J. Britt, J. Allen, and D. Bevy, "An integrated vehicle navigation system utilizing lane-detection and lateral position estimation systems in difficult environments for GPS," *IEEE Trans. Intell. Transp. Syst.*, vol. 15, no. 6, pp. 2615–2629, Dec. 2014.
- [10] D. Gruyer, R. Belaroussi, and M. Revilloud, "Accurate lateral positioning from map data and road marking detection," *Expert Syst. Appl.*, vol. 43, pp. 1–8, 2016.
- [11] T. Han, Y. Kim, and K. Kim, "Lane detection & localization for UGV in urban environment," in *Proc. Intell. Transp. Syst. Conf.*, 2014, pp. 590–596.
- [12] Z. Tao, P. Bonnifait, V. Frémont, and J. Ibañez-Guzman, "Mapping and localization using GPS, lane markings and proprioceptive sensors," in *Proc. IEEE/RSJ Int. Conf. Intell. Robots Syst.*, 2013, pp. 406–412.
- [13] P. Henkel and P. Burger, "Multi-Sensor fusion of GNSS receivers, inertial sensors and cameras for precise and reliable positioning," in *Proc. Conf. Future Automot. Technol.*, 2015, pp. 1–5.
- [14] P. G. Savage, "Strapdown analytics (part 1 and 2)," 2000.
- [15] P. G. Savage, "Strapdown inertial navigation integration algorithm design part 2: Velocity and position algorithms," *J. Guid. Control Dyn.*, vol. 22, pp. 384–384, 1998.
- [16] E. Shin, "Estimation techniques for low-cost inertial navigation," Ph.D. Thesis, Dept. Geomatics Eng., Univ. Calgary, Calgary, AB, Canada, May 2005.
- [17] G. Dissanayake, S. Sukkarieh, E. Nebot, and H. Durrant-Whyte, "The aiding of a low-cost strapdown inertial measurement unit using vehicle model constraints for land vehicle applications," *IEEE Trans. Robot. Automat.*, vol. 17, no. 5, pp. 731–747, Oct. 2001.
- [18] T. M. Hoang, N. R. Baek, S. W. Cho, K. W. Kim, and K. R. Park, "Road lane detection robust to shadows based on a fuzzy system using a visible light camera sensor," *Sensors*, vol. 17, 2017, Art. no. 2475.
- [19] R. Labayrade, J. Douret, J. Laneurit, and R. Chapuis, "A reliable and robust lane detection system based on the parallel use of three algorithms for driving safety assistance," *IEICE Trans. Inf. Syst.*, vol. 89, pp. 2092–2100, 2006.
- [20] Z. Kim, "Robust lane detection and tracking in challenging scenarios," *IEEE Trans. Intell. Transp. Syst.*, vol. 9, no. 1, pp. 16–26, Mar. 2008.
- [21] J. Ren, Y. Chen, L. Xin, and J. Shi, "Lane detection in video-based intelligent transportation monitoring via fast extracting and clustering of vehicle motion trajectories," *Math. Probl. Eng.*, vol. 2014, 2014, Art. no. 156296.
- [22] Y. Lee and H. Kim, "Real-time lane detection and departure warning system on embedded platform," in *Proc. IEEE 6th Int. Conf. Consum. Electron.*, 2016, pp. 1–4.
- [23] K. Kluge, "Extracting road curvature and orientation from image edge points without perceptual grouping into features," in *Proc. Intell. Veh. Symp.*, 1994, pp. 109–114.
- [24] H. J. Chu, G. J. Tsai, K. W. Chiang, and T. T. Duong, "GPS/MEMS INS data fusion and map matching in urban areas," *Sensors*, vol. 13, pp. 11280–11288, 2013.
- [25] W. Y. Ochieng, M. A. Quddus, and R. B. Noland, "Map-matching in complex urban road networks," *Revista Brasileira de Cartografia*, vol. 55, pp. 1–18, 2004.
- [26] M. Cossaboom, J. Georgy, T. Karamat, and A. Noureldin, "Augmented kalman filter and map matching for 3D RISS/GPS integration for land vehicles," *Int. J. Navig. Observ.*, vol. 2012, pp. 1–16, 2012.

Xiaoji Niu received the B.Eng. (Hons.) and the Ph.D. degrees in mechanical and electrical engineering from Tsinghua University, Beijing, China, in 1977 and 2002, respectively.

From 2003 to 2007, he was a Post Doctoral Fellow with the Mobile Multi-Sensor Systems Research Group, Department of Geomatics Engineering, University of Calgary. From 2007 to 2009, he was a Senior Scientist with SiRF Technology Inc. He is currently a Professor of GNSS Research Center, Wuhan University, Wuhan,



China. His research interests focus on GNSS/INS integration.



Yitang Peng received the Bachelor degree in navigation engineering from the School of Geodesy and Geomatics, Wuhan University, Wuhan, China, in 2017.

He currently works as a graduate student of GNSS Research Center, Wuhan University. His research interests include multisensory fusion for vehicle navigation and indoor positioning technology.



Chi Guo (Member, IEEE) received the M.Eng. and Ph.D. degrees in computer science from Wuhan University, Wuhan, China, in 2005 and 2010, respectively.

He is currently a Professor with the National Satellite Positioning System Engineering Technology Research Center, Wuhan University. His current research interests include BeiDou application, unmanned system navigation, and location based services.



Yuhang Dai received the B.Eng. degree (Hons.) in navigation engineering in 2020 from Wuhan University, Wuhan, China, where she is currently working toward the Master's degree in navigation, guidance, and control with GNSS Research Center.

Her main research interests include integration and visual-based navigation.



Quan Zhang (Member, IEEE) received the B.S. degree in geomatics engineering from Shandong University of Science and Technology, Qingdao, China in 2009, and the Ph.D. degree in geodesy and survey engineering from Wuhan University, Wuhan, China, in 2015.

From 2017 to 2018, he was a Post-Doctoral Researcher with the Digital Photogrammetry Research Group, Lyles School of Civil Engineering, Purdue University, West Lafayette, IN, USA.

He is currently an Associate Research Fellow of the GNSS Research Center, Wuhan University, Wuhan China. His research interests include inertial navigation and GNSS/INS integration technology.



Qijin Chen received the B.Eng. and Ph.D. degrees in geodesy and survey engineering from Wuhan University, Wuhan, China, in 2011 and 2016, respectively.

He is currently an Associate Research Fellow with the GNSS Research Center, Wuhan University, Wuhan, China. His research interests include INS with aiding and its applications in geodesy and precise surveying engineering including railway track geometry measuring and underground pipeline surveying.